

Characterization of the Hot Deformation Behavior of Cu–Cr–Zr Alloy by Processing Maps

Yi Zhang^{1,2,4} · Hui-Li Sun^{1,4} · Alex A. Volinsky² · Bao-Hong Tian^{1,4} · Zhe Chai^{1,3} · Ping Liu³ · Yong Liu^{1,4}

Received: 5 November 2015 / Revised: 30 December 2015 / Published online: 26 March 2016
© The Chinese Society for Metals and Springer-Verlag Berlin Heidelberg 2016

Abstract Hot deformation behavior of the Cu–Cr–Zr alloy was investigated using hot compressive tests in the temperature range of 650–850 °C and strain rate range of 0.001–10 s⁻¹. The constitutive equation of the alloy based on the hyperbolic-sine equation was established to characterize the flow stress as a function of strain rate and deformation temperature. The critical conditions for the occurrence of dynamic recrystallization were determined based on the alloy strain hardening rate curves. Based on the dynamic material model, the processing maps at the strains of 0.3, 0.4 and 0.5 were obtained. When the true strain was 0.5, greater power dissipation efficiency was observed at 800–850 °C and under 0.001–0.1 s⁻¹, with the peak efficiency of 47%. The evolution of DRX microstructure strongly depends on the deformation temperature and the strain rate. Based on the processing maps and microstructure evolution, the optimal hot working conditions for the Cu–Cr–Zr alloy are in the temperature range of 800–850 °C and the strain rate range of 0.001–0.1 s⁻¹.

KEY WORDS: Cu–Cr–Zr alloy; Hot deformation behavior; Strain hardening rate; Constitutive equation; Processing map

Available online at <http://link.springer.com/journal/40195>

✉ Yi Zhang
zhshgu436@163.com

✉ Alex A. Volinsky
volinsky@usf.edu

¹ School of Materials Science and Engineering, Henan University of Science and Technology, Luoyang 471003, China

² Department of Mechanical Engineering, University of South Florida, Tampa, FL 33620, USA

³ School of Materials Science and Engineering, University of Shanghai for Science and Technology, Shanghai 200093, China

⁴ Collaborative Innovation Center of Nonferrous Metals, Luoyang 471003, China

1 Introduction

Cu–Cr–Zr alloys are widely used as railway contact wires, connectors and lead frame materials in integrated circuits due to their excellent electrical conductivity and high strength [1–4]. In recent years, many investigations have been conducted to improve mechanical properties, thermal stability and electrical conductivity of the Cu–Cr–Zr alloys [5–7].

Hot workability of the Cu–Cr–Zr alloy, including strain hardening, dynamic recovery (DRV) and the dynamic recrystallization (DRX), is very important in industrial practice. In addition, the DRX kinetic model has been used to predict the DRX evolution during hot deformation processing [8, 9]. The processing maps based on the dynamic materials model (DMM) have been used to optimize the hot workability of the Cu–Cr–Zr alloys. Many investigations of the alloys hot deformation processing have been carried out. Zhang et al. [10] found that the addition of Ce can improve the deformation activation energy of the Cu–

0.4Cr–0.1Zr alloy during hot deformation. Ji *et al.* [11] found that the activation energy of the Cu–0.36Cr–0.03Zr alloy was 432.6 kJ/mol under the tested conditions. Ding *et al.* [12] studied the Cu–0.6Cr–0.03Zr alloy and found that the dynamic recrystallization developed completely at the hot deformation temperatures of 750 and 850 °C.

In order to optimize the hot workability of the Cu–Cr–Zr alloy, hot deformation behavior, strain hardening rate and processing maps of the Cu–Cr–Zr alloys were investigated in this study. The constitutive equation to obtain hot deformation activation energy for the flow behavior at elevated temperature was developed. The strain hardening rate for DRX of the alloy was determined to describe the dynamic recrystallization behavior. The processing maps based on the DMM model were derived to analyze the instability region and optimize the hot working parameters. Furthermore, the DRX nucleation mechanisms according to the microstructure evolution during hot compression process are also discussed.

2 Experimental

The chemical composition of the Cu–Cr–Zr alloy is: 0.4 wt% Cr, 0.1 wt% Zr and balanced of Cu. The alloy was melted in a vacuum induction furnace in argon. The cast ingot with diameter of 83 mm and length of 150 mm was homogenized at 930 °C for 2 h. Subsequently, the ingot was forged into 25-mm-diameter bars. Finally, the forged bars were solid solution-treated at 900 °C for 1 h, followed by water quenching.

The hot compression specimens were cut into cylinders with 8 mm diameter and 12 mm length. The specimens were compressed at a strain rate of 0.001–10 s^{−1} and deformation temperature of 650–850 °C using the Gleeble-1500D thermo-mechanical simulator. The cylindrical compression specimens were heated to the deformation temperature at 5 °C/s heating rate. Before deformation, all specimens were held under thermocouple-feedback-controlled AC current for 180 s to obtain uniform microstructure. All specimens were compressed to a true strain of 0.6 and immediately water-quenched from the test temperature to maintain deformation microstructure. The deformed specimens were sectioned parallel to the compression axis along the centerline direction. All specimens were polished and then etched with a solution of FeCl₃ (5 g) + C₂H₅OH (85 mL) + HCl (10 mL). The microstructure of the specimens was observed using an OLYMPUS PMG3 optical microscope and a JSM JEOL-5610LV scanning electron microscope (SEM). The samples for transmission electron microscopy (TEM) were prepared using Gatan 691 ion beam

thinner. The precipitated phase was characterized using a JEM-2100 (Joel, Japan) high-resolution transmission electron microscope (HRTEM).

3 Results and Discussion

3.1 Flow Stress Behavior

The true stress–true strain curves of isothermal compression of the Cu–Cr–Zr alloy at various strain rates and deformation temperatures are shown in Fig. 1. The flow stress is strongly dependent on the deformation temperature and the strain rate. The flow stress increased sharply with the strain at the early stage of deformation, and then reached a peak value (σ_p) when the alloy was deformed at 850 °C. This phenomenon happens because of the strain hardening caused by dislocation multiplication [13]. After the peak flow stress, the flow stress decreased gradually and then reached a steady state. With the increase of strain, the DRX instead of DRV happened after the critical density of dislocations was obtained. Subsequently, a balance between strain hardening and flow softening was achieved. Thus, the flow stress of the alloy exhibited steady state characteristics. According to Fig. 1, typical continuous strain hardening was observed at the deformation temperatures of 650 and 700 °C, respectively. It is a typical dynamic recovery (DRV) behavior at lower temperatures and higher strain rates. The reason is that there was not enough time for energy accumulation and dislocation annihilation at higher strain rates and lower temperatures [14]. The effects of deformation temperature and strain rate on the peak flow stress (σ_p) of the Cu–Cr–Zr alloy are shown in Fig. 2. It can be seen that the peak flow stress decreased with the deformation temperature at a given strain rate and increased with the strain rate at a constant deformation temperature. This indicates that the Cu–Cr–Zr alloy has negative temperature sensitivity and positive strain rate sensitivity [15].

3.2 Activation Energy and Constitutive Equations

During the process of hot deformation, the relationship between the flow stress, the strain rate and the deformation temperature can be represented by the Zener–Hollomon (Z) parameter expressed as [16–18]:

$$Z = \dot{\epsilon} \exp\left(\frac{Q}{RT}\right). \quad (1)$$

At high and low stress, the strain rate could be expressed by the following equations, respectively:

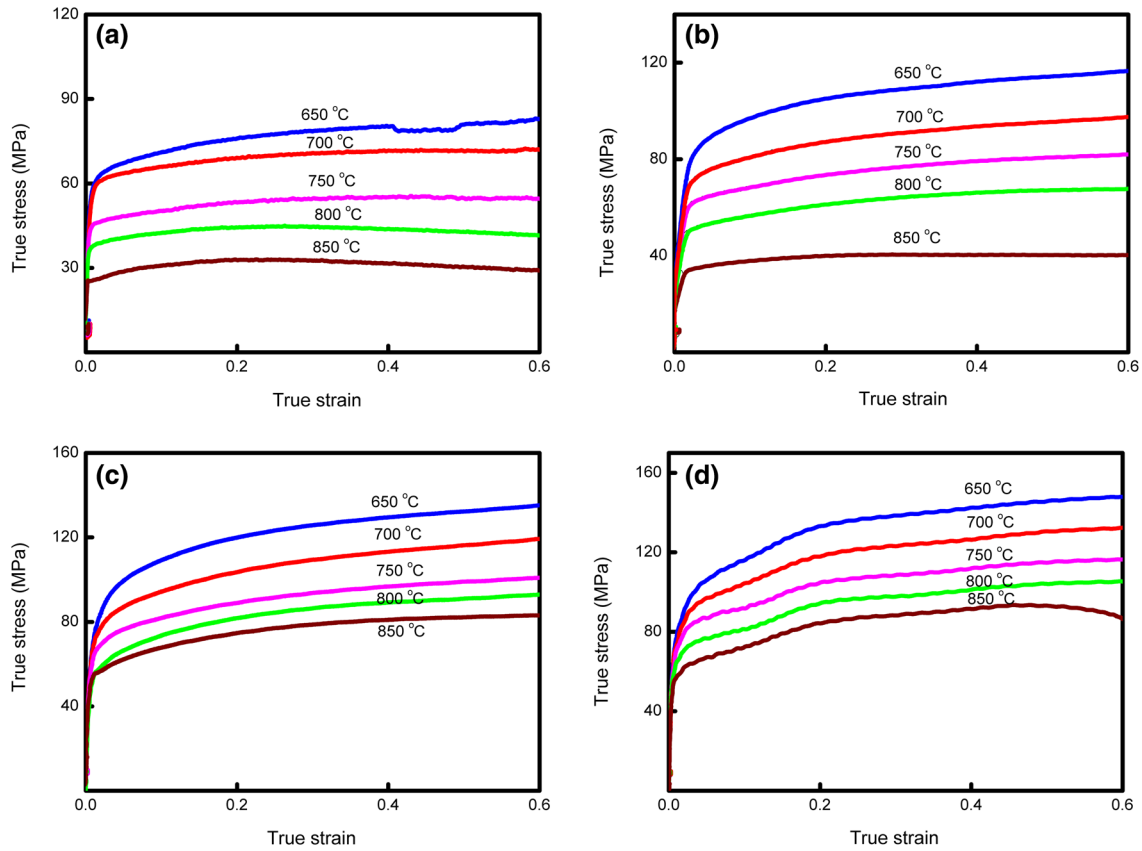


Fig. 1 True stress–true strain curves of the Cu–Cr–Zr alloy deformed at different strain rates: **a** $\dot{\epsilon} = 0.001 \text{ s}^{-1}$, **b** $\dot{\epsilon} = 0.1 \text{ s}^{-1}$, **c** $\dot{\epsilon} = 1 \text{ s}^{-1}$, **d** $\dot{\epsilon} = 10 \text{ s}^{-1}$

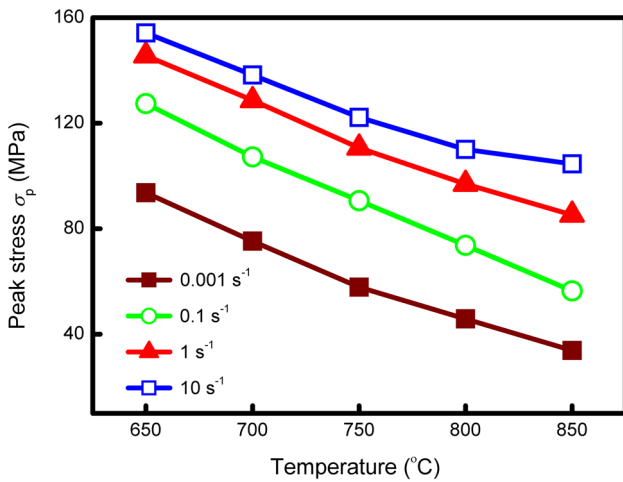


Fig. 2 Relationship between the peak stress and deformation temperature under different strain rates

$$\dot{\epsilon} = A_1 \sigma^{n_1} \exp\left(-\frac{Q}{RT}\right). \tag{2}$$

$$\dot{\epsilon} = A_2 \exp(\beta\sigma) \exp\left(-\frac{Q}{RT}\right). \tag{3}$$

Over a wide range, the equation can be expressed as:

$$\dot{\epsilon} = A [\sinh(\alpha\sigma)]^n \exp\left(-\frac{Q}{RT}\right). \tag{4}$$

where $\dot{\epsilon}$ is the strain rate (s^{-1}), Q is the activation energy of DRX (kJ/mol), R is the universal gas constant ($8.314 \text{ J mol}^{-1} \text{ K}^{-1}$), T is the absolute temperature (K), σ is the flow stress (MPa) for a given strain, A (s^{-1}), A_1 , A_2 , n_1 , n and α (MPa^{-1}) are the materials constants (where $\alpha = \beta/n_1$). Taking natural logarithms of both sides of Eq. (2) and Eq. (3) yields:

$$\ln \dot{\epsilon} = \ln A_1 + n_1 \ln \sigma - \frac{Q}{RT}. \tag{5}$$

$$\ln \dot{\epsilon} = \ln A_2 + \beta\sigma - \frac{Q}{RT}. \tag{6}$$

A linear relationship exists between $\ln \dot{\epsilon}$ and $\ln \sigma$ with the linear slope n_1 , as shown in Fig. 3a. A linear relationship also exists between $\ln \dot{\epsilon}$ and σ with the linear slope β , as shown in Fig. 3b. The values of n_1 and β can be calculated from the average values of the slopes: $n_1 = 7.558$, $\beta = 0.128$. Thus, the α value of the alloy is

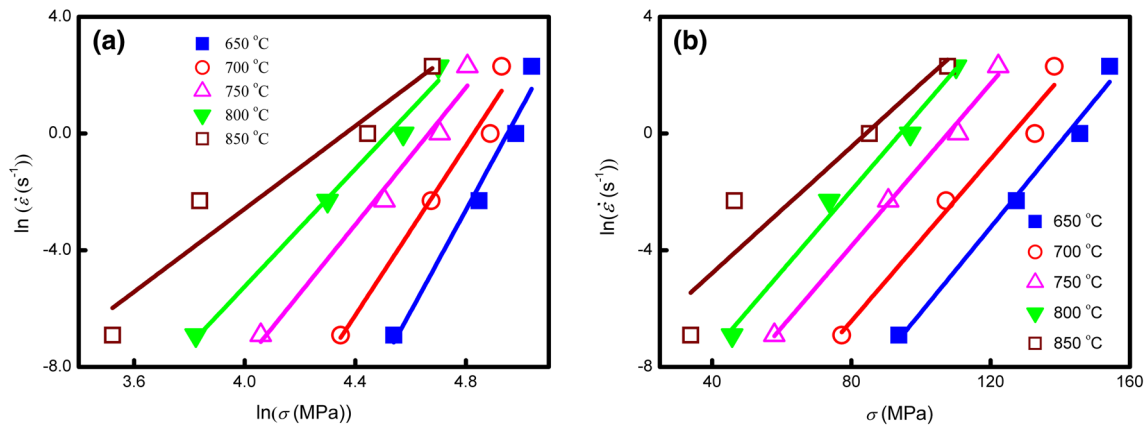


Fig. 3 Relationships between $\ln \dot{\epsilon}$ and $\ln \sigma$ **a**, $\ln \dot{\epsilon}$ and σ **b**

calculated as $\alpha = \beta/n_1 = 0.017 \text{ MPa}^{-1}$. Taking natural logarithms of both sides of Eq. (4) yields:

$$\ln \dot{\epsilon} = \ln A + n \ln[\sinh(\alpha\sigma)] - \frac{Q}{RT}. \quad (7)$$

Taking partial differentials of Eq. (7) into consideration yields:

$$Q = R \left[\frac{\partial(\ln \dot{\epsilon})}{\partial \ln[\sinh(\alpha\sigma)]} \right]_T \left[\frac{\partial \ln[\sinh(\alpha\sigma)]}{\partial (1/T)} \right]_{\dot{\epsilon}} = RnS. \quad (8)$$

According to Eq. (8), the plots of $\ln \dot{\epsilon} - \ln[\sinh(\alpha\sigma)]$ and $\ln[\sinh(\alpha\sigma)] - 1/T$ at different temperatures are shown in Fig. 4a, b, respectively. Consequently, the values of n and S can be calculated by means of linear regression analysis, and then the value of Q can be determined as $Q = RnS = 392.48 \text{ kJ/mol}$.

The Q value of this alloy is a little lower than that of the Cu–0.4Cr–0.15Zr–0.05Ce alloy (495.8 kJ/mol), Cu–0.36Cr–0.03Zr alloy (432.6 kJ/mol) and the Cu–0.6Cr–0.03Zr alloy (572.053 kJ/mol), based on Refs. [10–12]. Comparing the activation energy Q of the Cu–Cr–Zr with that in Ref. [10], the Q increased by 21% with the addition of Ce. The reason is that the Ce can fix dislocations at the grain boundary and maintain high dislocation density. Thus, the addition of Ce can increase the deformation activation energy with more difficult dynamic recovery. A higher strain rate (20 s^{-1}) was applied in the previous work [11]. If the strain rate is too high, there is not enough time for DRX, so much greater activation energy Q is needed. It was found that the alloying elements play an important role in increasing the activation energy [19]. The Cu–0.6Cr–0.03Zr alloy used in Ref. [12] has higher contents of Cr and Zr alloying elements than the current Cu–0.4Cr–0.1Zr alloy, and solution strengthening caused by these alloying elements may give rise to higher activation energy. The higher the activation energy Q , the harder the hot deformation of the alloy [20]. Thus, the hot workability

is harder if the alloy has higher activation energy Q for hot deformation. This indicates that dislocation movement and DRX are easier to occur for this experimental alloy. It also means that this experimental alloy has good hot workability.

Taking natural logarithms of both sides of Eq. (4) yields:

$$\ln Z = \ln A + n \ln[\sinh(\alpha\sigma)]. \quad (9)$$

where $\ln A$ is the intercept of the $\ln[\sinh(\alpha\sigma)]$ and $\ln Z$ plot, as shown in Fig. 5. The value of A is 4.929×10^{16} . Thus, the constitutive equation of the Cu–Cr–Zr alloy in the hyperbolic-sine function can be expressed as:

$$\dot{\epsilon} = 4.929 \times 10^{16} [\sinh(0.017\sigma)]^{7.558} \exp(-392.48/RT). \quad (10)$$

3.3 Strain Hardening Behavior

The strain hardening rate θ ($d\sigma/d\epsilon$) has been widely used to investigate the critical strain for the DRX onset. Three typical stages of the flow curves for different strain hardening features have been determined as: $\theta > 0$ for the strain hardening stage, $\theta < 0$ for the continuously decreasing stage and $\theta = 0$ for the steady state [21]. The effects of temperature, strain rate and strain on the strain hardening rate θ ($d\sigma/d\epsilon$) are shown in Fig. 6. It can be seen that the strain hardening rate has a sharp drop before reaching a plateau. The slope of the strain hardening rate at 850 °C is much steeper than that at other temperatures. Negative values of the strain hardening rate are observed in Fig. 6, except for the 650 °C. A negative value of the strain hardening rate is associated with the flow softening due to the occurrence of DRX. Thus, the minimum value of θ corresponds with the maximum softening rate [22]. The inflection point is marked by an arrow in Fig. 6 and is clear for the critical strain ϵ_c of the alloy deformed at 850 °C

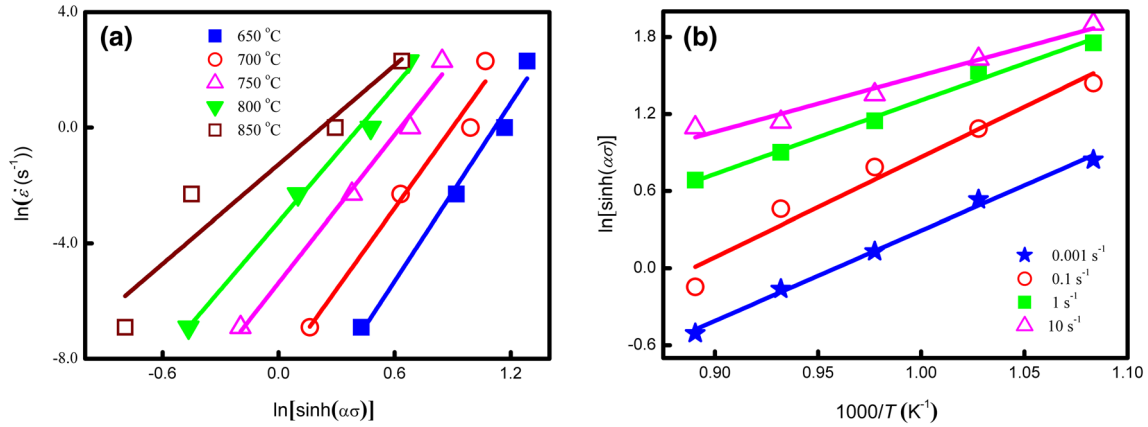


Fig. 4 Relationship between $\ln[\sinh(\alpha\sigma)]$ and $\ln \dot{\epsilon}$ a, $\ln[\sinh(\alpha\sigma)]$ and $1000/T$ b

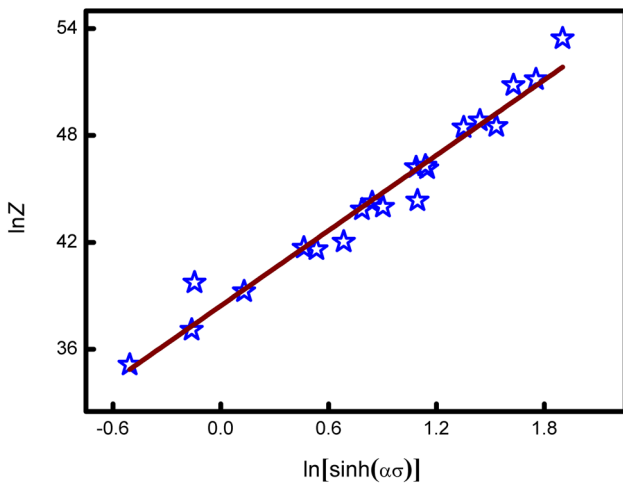


Fig. 5 Zener–Hollomon parameter, Z , as a function of the flow stress

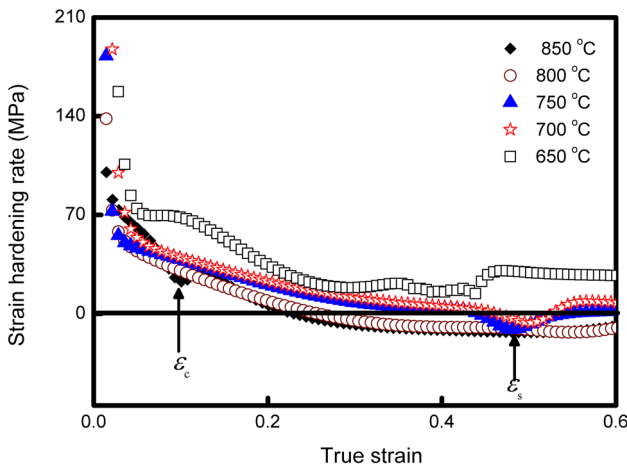


Fig. 6 Strain hardening rate variation of the Cu–Cr–Zr alloy under different deformation temperature at the true strain of 0.001 s^{-1}

with the strain rate of 0.001 s^{-1} . A minimum value of θ was observed in Fig. 6 at $850 \text{ }^\circ\text{C}$ and reflects the maximum softening rate at ϵ_s .

3.4 Processing Maps

The processing map based on dynamic materials model (DMM) developed by Prasad *et al.* [23] has been used to optimize hot workability. In the DMM model, the hot deformation process was considered as a power system and the workpiece was a power dissipater under hot deformation [24]. The instantaneous power dissipated (P) may be separated into two complementary parts during plastic deformation: dissipative quantity (G) and dissipation of association (J), mathematically defined as:

$$P = J + G = \sigma \dot{\epsilon} = \int_0^\sigma \dot{\epsilon} d\sigma + \int_0^{\dot{\epsilon}} \sigma d\dot{\epsilon}. \tag{11}$$

In this model, G and J can be determined from the parameter m , which represents the strain rate sensitivity coefficient of the material. It can be expressed as:

$$m = \left(\frac{\partial J}{\partial G} \right)_{\epsilon, T} = \left[\frac{\partial(\ln \sigma)}{\partial(\ln \dot{\epsilon})} \right]_{\epsilon, T}. \tag{12}$$

For an ideal linear dissipation process, $m = 1$ and $J = J_{\max} = \sigma \dot{\epsilon} / 2 = P / 2$, and the value of J can be obtained from a dimensionless parameter, called the efficiency of power dissipation, defined as:

$$\eta = \frac{J}{J_{\max}} = \frac{2m}{m + 1}. \tag{13}$$

A continuum instability criterion is developed based on the extremum principles of irreversible thermodynamics, which can be expressed as [25]:

$$\xi(\dot{\epsilon}) = \frac{\partial \ln\left(\frac{m}{m+1}\right)}{\partial \ln \dot{\epsilon}} + m < 0. \quad (14)$$

The variation of the instability parameter $\xi(\dot{\epsilon})$ as a function of temperature and strain rate can be expressed by the instability map.

The processing maps of the Cu–Cr–Zr alloy deformed at the strain of 0.3, 0.4 and 0.5 are shown in Fig. 7a–c, respectively. The contours represent the efficiency of power dissipation marked as percent, while the shaded areas indicate the flow unstable domains. It can be seen that the distribution characteristics of the power dissipation are similar, but the shaded domains area increased with strain. In all figures, similar shaded domains were observed at the deformation temperature of 830–850 °C. When the strain is 0.4, the flow instability regions consist of four parts: One is in the high temperature regions, and other three are in the high strain rate regions. At the strain of 0.5 domain A has a stable region with a peak efficiency of power dissipation shown in Fig. 7c, which corresponds to the samples deformed at higher temperatures and lower strain rates. It revealed a greater efficiency of power dissipation in the temperature range of 800–850 °C and the strain rate range of 0.001–0.1 s⁻¹, with a peak efficiency of 47% at 840 °C and 0.01 s⁻¹. The value η is higher, and the workability is better in this deformation domain. This demonstrates that the material deformed at these conditions with high efficiency of power dissipation shows good workability [26]. At the strain of 0.5, two instability domains were observed in the processing map: domain B occurs in the temperature range of 650–850 °C and the strain rate range of 1–10 s⁻¹. Domain C occurs in the temperature range of 830–850 °C and strain rate range of 10⁻⁴–10⁻⁶ s⁻¹. Hot working in these regions is considered to be unsafe. According to the processing maps of the Cu–Cr–Zr alloy, the optimal hot working conditions are in the temperature range of 800–850 °C and strain rate range of 0.001–0.1 s⁻¹.

3.5 Microstructure Evolution

Optical images of the Cu–Cr–Zr alloy microstructure deformed at different deformation conditions are shown in Fig. 8. According to Fig. 8a, the original grains were elongated. There are no obvious recrystallized grains observed, except for the shear zone when deformed at the temperature of 700 °C and the strain rate of 0.1 s⁻¹, as seen in Fig. 8b. The main softening mechanism is dynamic recovery. The microstructure of the alloy deformed at 750 °C and 0.001 s⁻¹ is shown in Fig. 8c. It can be seen that there is a large amount of refined recrystallized grains around original grain boundaries. Meanwhile, the serrated grain boundaries marked by the arrows are observed in Fig. 8c. The inset shows the corresponding magnified serrated grain boundary. It indicates that the dynamic recrystallization occurred. However, some elongated grains are still present at the deformed microstructure. This means that the dynamic recrystallization was not completed. Here, all microstructure consists of mixed grains. The number of dynamic recrystallization grains increases with the temperature, as seen in Fig. 8d. Figure 8e shows the microstructure of the sample deformed at 800 °C and 0.001 s⁻¹. All the original grains are replaced by the new DRX grains, indicating that the dynamic recrystallization process is complete. Subsequently, the recrystallized grains grew in size, as seen in Fig. 8f. It can be seen that the recrystallized grains are still fine and homogenized distribution.

SEM images of the alloy deformed at the strain rate of 10 s⁻¹ and 650 °C, 700 °C temperatures are shown in Fig. 9a, b, respectively. It can be seen that the cracks marked by the arrows appeared in the alloy at these deformation conditions. The instability mechanisms are associated with cracking at low temperature and high strain rate [27]. This is in good agreement with the processing maps results. Therefore, the alloy can easily fracture during deformation processing. These deformation conditions and corresponding microstructure should be avoided in

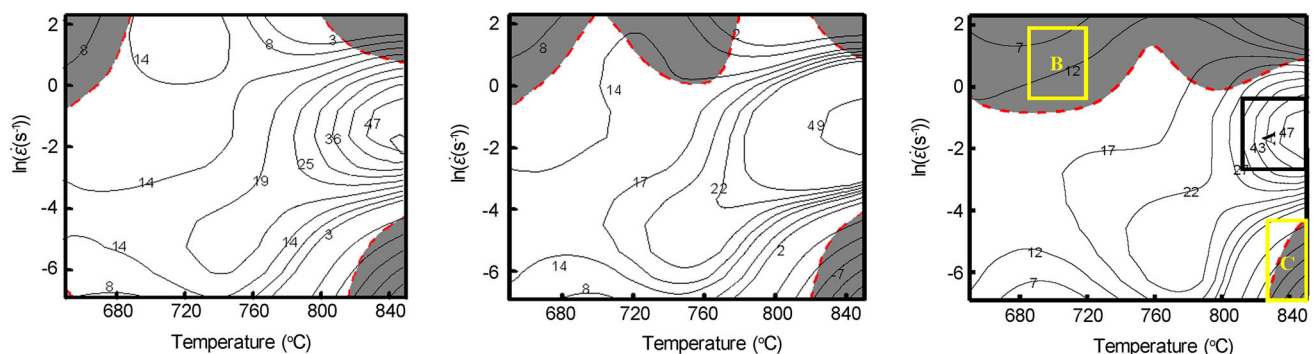


Fig. 7 Processing maps for the Cu–Cr–Zr alloy deformed at the true strain of 0.3 **a**, 0.4 **b**, 0.5 **c**

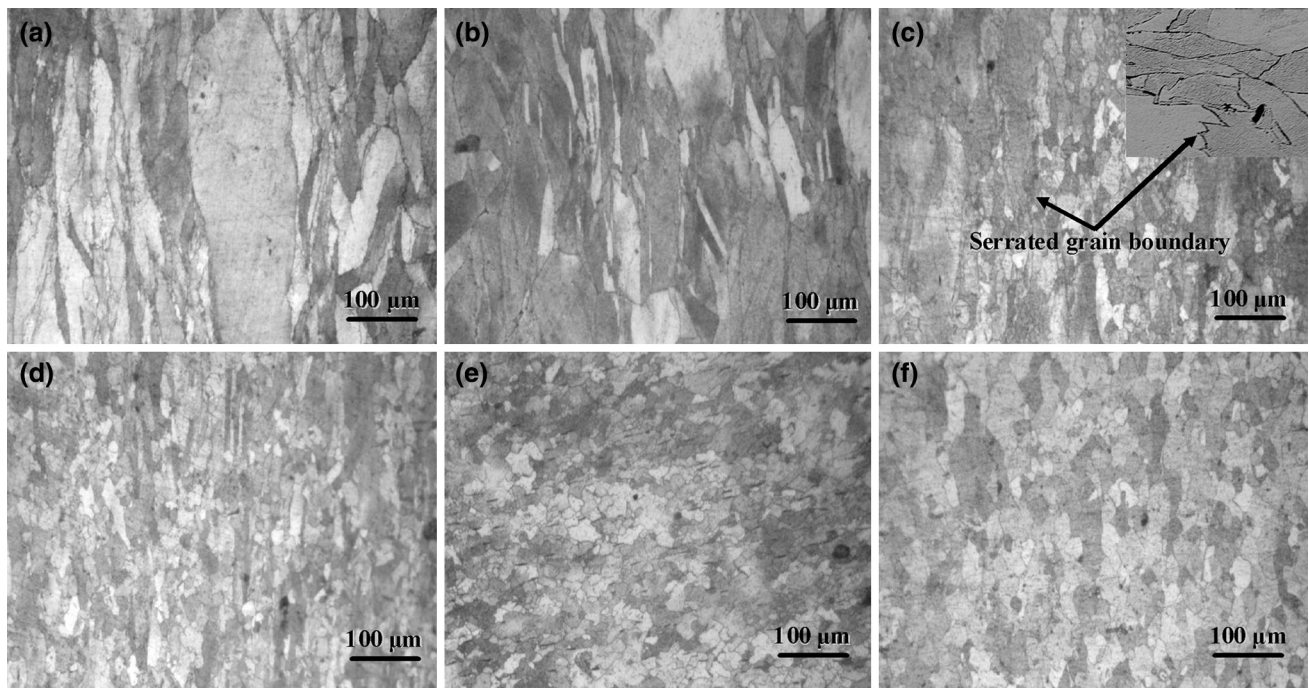


Fig. 8 Optical micrographs of the microstructure of the hot compressed specimens deformed at different temperatures and strain rates: **a** 650 °C, 0.1 s⁻¹; **b** 700 °C, 0.1 s⁻¹; **c** 750 °C, 0.001 s⁻¹; **d** 800 °C, 0.01 s⁻¹; **e** 800 °C, 0.001 s⁻¹; **f** 850 °C, 0.001 s⁻¹

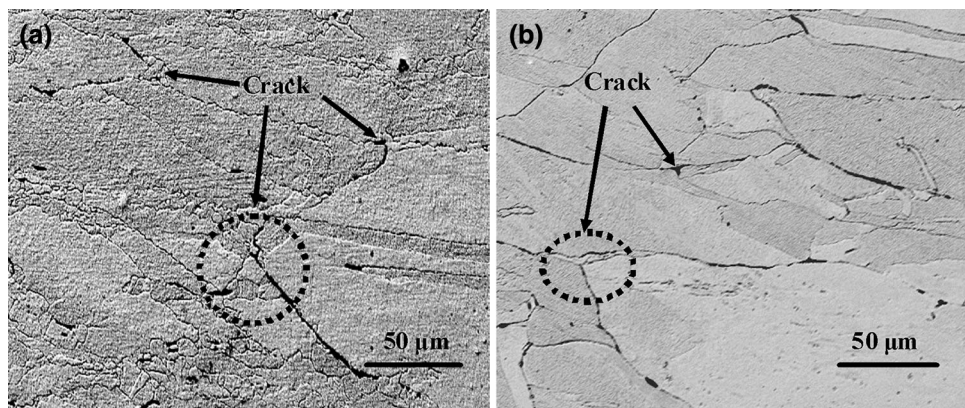


Fig. 9 SEM images showing cracks in the compressed specimen at different temperatures and strain rates: **a** 650 °C, 10 s⁻¹; **b** 700 °C, 10 s⁻¹

industrial practice. Thus, the optimal processing parameters for hot deformation of the Cu–Cr–Zr alloy are: temperature range of 800–850 °C and strain rate range of 0.001–0.1 s⁻¹.

TEM micrographs of the Cu–Cr–Zr alloy deformed at various deformation conditions are shown in Fig. 10. The banded structures were observed at low temperature and high strain rate in Fig. 10a, b, respectively. It can be seen that the dislocations are tangled and stored in the grains interior of the alloy at 700 °C and 0.001 s⁻¹ strain rate in Fig. 10c. According to this microstructure, no dynamic recrystallization grains were observed. This

is because that there is not enough energy for dislocation annihilation at low deformation temperature and high strain rate [28]. Therefore, the dynamic recovery is the main softening mechanism. The nucleation of dynamically recrystallized grains appears at the high-angle grain boundaries marked by the dashed lines in Fig. 10d, indicating DRX occurrence at high temperature and low strain rate. Selected-area diffraction patterns obtained from the precipitates are shown in Fig. 10e. Therefore, it can be concluded that the deformation temperature and strain rate can strongly affect the deformed microstructure.

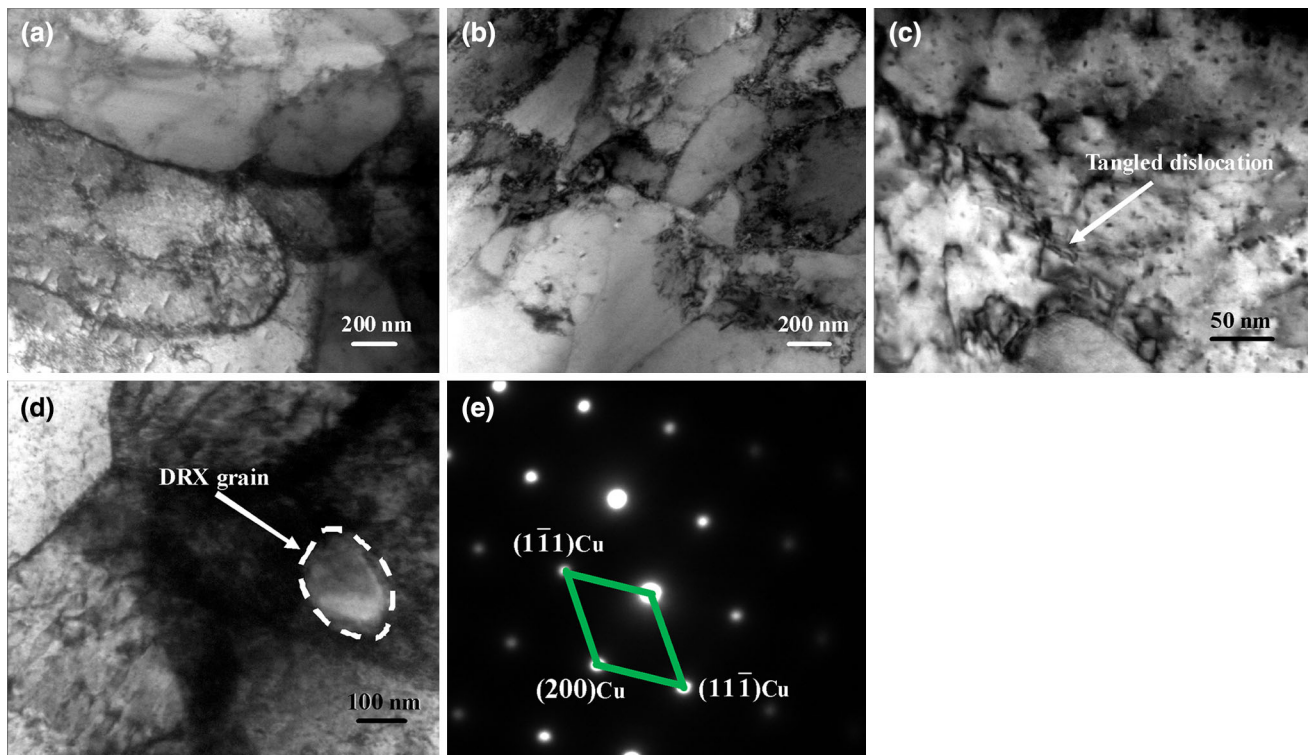


Fig. 10 TEM micrographs of the Cu–Cr–Zr alloy deformed at different temperatures and strain rates: **a** 650 °C and 10 s⁻¹; **b** 700 °C and 0.1 s⁻¹; **c** 700 °C and 0.001 s⁻¹; **d** 800 °C and 0.001 s⁻¹; **e** selected-area diffraction pattern from **d**

4 Conclusions

1. The apparent activation energy for hot deformation of the Cu–Cr–Zr alloy is 392.48 kJ/mol. The constitutive equation for the flow stress can be expressed as: $\dot{\epsilon} = 4.929 \times 10^{16} [\sinh(0.017\sigma)]^{7.558} \exp(-392.48/RT)$.
2. The critical strains ϵ_c and ϵ_s of the alloy deformed at 850 °C with the strain rate of 0.001 s⁻¹ were obtained from the strain hardening rate θ .
3. The processing maps at 0.3, 0.4 and 0.5 strain were established based on the DMM model principles. The peak efficiency is about 49%, and the Cu–Cr–Zr alloy optimal hot working conditions are in the temperature range of 800–850 °C and the strain rate range of 0.001–0.1 s⁻¹.
4. The deformation temperature and strain rate can strongly affect the deformed microstructure. Dynamic recrystallization appears at high temperature and low strain rate. Cracks were observed at low deformation temperature and high strain rate.

Acknowledgments This work was financially supported by the National Natural Science Foundation of China (No. 51101052) and the National Science Foundation (No. IRES 1358088).

References

- [1] J.H. Su, H.J. Li, Q.M. Dong, P. Liu, B.X. Kang, B.H. Tian, *Acta Metall. Sin. (Engl. Lett.)* **17**, 741 (2004)
- [2] S.G. Mu, F.A. Guo, Y.Q. Tang, X.M. Cao, M.T. Tang, *Mater. Sci. Eng. A* **475**, 235 (2008)
- [3] D.D. Qu, Z.J. Zhou, Y.J. Yum, J. Aktaa, *J. Nucl. Mater.* **455**, 130 (2014)
- [4] Y. Pang, C.D. Xia, M.P. Wang, Z. Li, Z. Xiao, H.G. Wei, X.F. Sheng, Y.L. Jia, C. Chen, *J. Alloys Compd.* **582**, 786 (2014)
- [5] K.M. Liu, Z.Y. Jiang, J.W. Zhao, J. Zou, L. Lu, D.P. Lu, *Metall. Mater. Trans. A* **46**, 2255 (2015)
- [6] Y.A. Wang, J.X. Li, Y. Yan, L.J. Qiao, *Tribol. Int.* **50**, 26 (2012)
- [7] C.D. Xia, Y.L. Jia, W. Zhang, K. Zhang, Q.Y. Dong, G. Xu, M.P. Wang, *Mater. Des.* **39**, 404 (2012)
- [8] D.G. Cram, H.S. Zuro, Y.J.M. Brechet, C.R. Hutchinson, *Acta Mater.* **57**, 5218 (2009)
- [9] G. Wang, L. Xu, Y. Wang, Z. Zheng, Y.Y. Cui, R. Yang, *J. Mater. Sci. Technol.* **27**, 893 (2011)
- [10] Y. Zhang, A.A. Volinsky, H.T. Tran, Z. Chai, P. Liu, B.H. Tian, *J. Mater. Eng. Perform.* **24**, 3783 (2015)
- [11] G.L. Ji, Q. Li, K.Y. Ding, L. Yang, L. Li, *J. Alloys Compd.* **648**, 397 (2015)
- [12] Z.Y. Ding, S.G. Jia, P.F. Zhao, M. Deng, K.X. Song, *Mater. Sci. Eng. A* **570**, 87 (2013)
- [13] M.H. Wang, Y.F. Li, W.H. Wang, J. Zhou, A. Chiba, *Mater. Des.* **45**, 384 (2013)
- [14] D.J. Li, Y.R. Feng, S.Y. Song, Q. Liu, Q. Bai, F.Z. Ren, F.S. Shanguan, *J. Alloys Compd.* **618**, 768 (2015)

- [15] F.T. Kong, N. Cui, Y.Y. Chen, X.P. Wang, N.N. Xiong, *Intermetallics* **55**, 66 (2014)
- [16] G. Zhou, H. Ding, F.R. Cao, B.J. Zhang, *J. Mater. Sci. Technol.* **30**, 217 (2014)
- [17] A.D. Manshadi, M.R. Barnett, P.D. Hodgson, *Metall. Mater. Trans. A* **39**, 1359 (2008)
- [18] Z.Y. Zeng, L.Q. Chen, F.X. Zhu, X.H. Liu, *J. Mater. Sci. Technol.* **27**, 913 (2011)
- [19] N.P. Jin, H. Zhang, Y. Han, W.X. Wu, J.H. Chen, *Mater. Charact.* **60**, 530 (2009)
- [20] H.J. McQueen, S. Yue, N.D. Ryan, E. Fry, *J. Mater. Process. Technol.* **53**, 293 (1995)
- [21] Y.Q. Ning, X. Luo, H.Q. Liang, H.Z. Guo, J.L. Zhang, K. Tan, *Mater. Sci. Eng. A* **635**, 77 (2015)
- [22] A. Etaati, K. Dehghani, *Mater. Chem. Phys.* **140**, 208 (2013)
- [23] Y.V.R.K. Prasad, T. Seshacharyulu, *Mater. Sci. Eng. A* **243**, 82 (1998)
- [24] L. Wang, F. Liu, J.J. Cheng, Q. Zuo, C.F. Chen, *J. Alloys Compd.* **623**, 69 (2015)
- [25] T.D. Kil, J.M. Lee, Y.H. Moon, *J. Mater. Process. Technol.* **220**, 224 (2015)
- [26] Q.L. Pan, B. Li, Y. Wang, Y.W. Zhang, Z.M. Yin, *Mater. Sci. Eng. A* **585**, 371 (2013)
- [27] B.J. Lv, J. Peng, L.L. Zhua, Y.J. Wang, A.T. Tang, *Mater. Sci. Eng. A* **599**, 150 (2014)
- [28] W.Y. Liu, H. Zhao, D. Li, Z.Q. Zhang, G.J. Huang, Q. Liu, *Mater. Sci. Eng. A* **596**, 176 (2014)